Nanoscale

PAPER

View Article Online
View Journal | View Issue

Cite this: *Nanoscale*, 2024, **16**, 3061

Unveiling transient current response in bilayer oxide-based physical reservoirs for time-series data analysis†

Bo-Ru Lai,[a] Kuan-Ting Chen,[a] Rajneesh Chaurasiya,[a,b] Song-Xian You,[a] Wen-Dung Hsu[a] and Jen-Sue Chen *[a,c]

Received 26th October 2023,
Accepted 12th January 2024

DOI: 10.1039/d3nr05401b

rsc.li/nanoscale

Physical reservoirs employed to map time-series data and analyze extracted features have attracted interest owing to their low training cost and mitigated interconnection complexity. This study reports a physical reservoir based on a bilayer oxide-based dynamic memristor. The proposed device exhibits a nonlinear current response and short-term memory (STM), satisfying the requirements of reservoir computing (RC). These characteristics are validated using a compact model to account for resistive switching (RS) *via* the dynamic evolution of the internal state variable and the relocation of oxygen vacancies. Mathematically, the transient current response can be quantitatively described according to a simple set of equations to correlate the theoretical framework with experimental results. Furthermore, the device shows significant reliability and ability to distinguish 4-bit inputs and four diverse neural firing patterns. Therefore, this work shows the feasibility of implementing physical reservoirs in hardware and advances the understanding of the dynamic response.

Introduction

Artificial neural networks (ANNs) are designed to mimic the structure and functionality of biological neural networks found in the human brain.[1–3] The nervous system comprises billions of interconnected neurons that communicate *via* electrical and chemical signals.[4,5] These neurons are organized into complex networks that can process and integrate a vast amount of information, learn from experience, and adapt to new situations.[6] ANNs have shown potential in object identification,[7] bioinformatics,[8] and speech recognition.[9] They have even outperformed humans in some applications, such as generative pretrained transformer 3 (GPT-3)[10] and AlphaGo.[11] ANNs are generally divided into two types: feedforward neural networks (FNNs) and recurrent neural networks (RNNs). FNNs facilitate unidirectional information flow without incorporating loops, whereas RNNs feature feedback connections that enable information propagation not only from the input layer to the output layer but also within the hidden layers. This recurrent structure makes RNNs particularly well-suited for processing time-series data, as they can capture temporal dependencies and model sequential patterns effectively.[12,13] However, the training of RNNs poses challenges because of exploding or vanishing gradients in recurrent structures. This difficulty in training RNNs necessitates significant computational power and cost.[14] Reservoir computing (RC) system has the potential to overcome these problems because a smaller neural network and a simpler weight update rule can be used compared with RNNs.[15,16] At the software level, RC systems have demonstrated satisfactory performance in speech recognition[17] and time-series prediction.[18,19]

Physical reservoir computing (PRC)[20–22] has recently attracted interest as it can significantly reduce computational resources needed for time-series data processing. PRC comprises two parts: (1) the physical reservoir, which acts as a nonlinear transformation of the input data, enhancing the separability and discriminative capabilities of the input data by mapping it to a feature space and (2) the readout layer, which is a small network and linearly processes the data output from the physical reservoir. One of the main advantages of PRC is the reduced computational cost due to the training of only the weights in the readout layer because the physical reservoir itself does not require weight updating. This characteristic

[a]*Department of Materials Science and Engineering, National Cheng Kung University, Tainan 70101, Taiwan. E-mail: jenschen@ncku.edu.tw*
[b]*Department of Electronics and Communication Engineering, Amrita School of Engineering, Amrita Vishwa Vidyapeetham, Chennai, India*
[c]*Academy of Innovative Semiconductor and Sustainable Manufacturing, National Cheng Kung University, Tainan 70101, Taiwan*
† Electronic supplementary information (ESI) available. See DOI: https://doi.org/10.1039/d3nr05401b

makes the implementation of the physical reservoir in hardware more feasible. Various physical reservoirs have been reported to meet these requirements.[20,21,23] Moreover, the 4-bit sequential coding for handwritten digits classification and compression of spatial dimension for feature space extraction through volatile memristive devices were revealed.[24,25] Milano *et al.* demonstrated a bottom-up approach in constructing low-cost computing paradigm through self-organized nanowire networks for mapping the spatio-temporal inputs.[26] In addition to the volatile memristor-based physical reservoir, the subsequent readout layer constructed by the 1T1R (1 Transistor 1 Memristor) crossbar array is also explored. Midya *et al.* utilized the formal readout layer which employs backpropagation-based supervised learning to train the weights by modulating the 1T1R conductance state.[27] Apart from the backpropagation processing, the spiking neuromorphic system was also established in the work of Matsukatova *et al.* to perform computation based on the spike-timing-dependent plasticity learning rule with low-power spiking signals.[28]

In this study, we demonstrate a physical reservoir based on the bilayer oxide-based dynamic memristor, which utilizes an oxide interface instead of the conductive filament-based mechanism and functions as a nonlinear dynamical system with short-term memory (STM). The platinum (Pt) is selected as the bottom electrode for its high work function to form Schottky barrier with most of the oxide semiconductors and dielectrics.[29,30] The bottom oxide layer, tantalum oxide (TaO_x), is a wide bandgap material and it possesses high oxygen vacancies mobility due to the relatively low activation barrier of oxygen vacancies for migration.[31,32] For the top oxide materials, compared with TaO_x, indium gallium zinc oxide (IGZO) exhibits higher electronic affinity and lower bandgap.[33,34] The low-work function metal Ta is employed as the top electrode to form an Ohmic contact between the IGZO/Ta interface.[35,36] This heterojuction memristor accounts for the resistive switching and the asymmetric Schottky barrier and induces the self-rectification behavior. Different from other related studies that mainly emphasized on implementing specific physical reservoir functions and applications on time-series data processing in memristor-based RC,[37–39] the preeminent discussion in this study is the compact model, which incorporates the dynamic evolution of the internal state variable (w) and enables the quantification of transient current response. Because of the consideration of the w, the conduction status in the memristor can be acquired when the electrical stimulation is removed and back to zero voltage. This allows the device behavior to be predicted accurately and facilitate the simulation platform to perform time series data classification in reservoir computing system.[40,41] We provide an explanation for the fundamental driving mechanisms behind the observed intrinsic nonlinear characteristics and STM effects of the dynamic memristor. The simulation results are well-aligned with the experimentally measured device characteristics, which can be further integrated into the RC framework. Additionally, compared to the recently reported studies, the proposed dynamic memristor exhibits higher On/Off ratio and rectification ratio, possessing the potential for superior integration density and efficient operation of the reservoir system.[42,43] The comparison of these electrical characteristics of related studies is provided in Table S1.† The use of the bilayer oxide to form a heterojunction offers a promising approach to memristor fabrication for future neuromorphic technologies. Additionally, the simulation work lays the foundation for the optimization of bilayer oxide-based dynamic memristors and the application in dynamic signal processing.

Results and discussion

Microstructural characterization and electrical response

In this study, we implemented a bilayer oxide-based dynamic memristor with indium gallium zinc oxide (IGZO) stacking on tantalum oxide (TaO_x). The experimental details of the device are discussed in the methods section. The left panel of Fig. 1a illustrates the stacking of layers, including their respective thicknesses, whereas the right panel shows the corresponding transmission electron microscopy (TEM) image of the device. Throughout the electrical measurements, the top electrode (TE), Ta, is maintained at ground potential while the voltage is applied to the bottom electrode (BE), Pt. Fig. 1b demonstrates an asymmetric current–voltage (I–V) hysteresis curve during the voltage scan (−4.0 V → 0.0 V → 4.0 V → 0.0 V → −4.0 V). The I–V curve is also measured for more than 100 scans, as shown in Fig. S1,† indicating the stability and reliability of the device. At low applied voltages (under 2 V), the current is hindered by the Schottky contact (Pt/TaO_x).[44,45] In addition, the observed hysteresis loop confirms the presence of memristive switching within the device. This effect is further demonstrated by pulse measurement, as shown in Fig. 1c. The device initially exhibits an HRS during the first small pulse while the current constantly increases over time during the programming pulse (3 V, 5 ms). Notably, after the strong stimulus, the device exhibits the discernible current response during the latter small pulses, indicating the potential for transition from HRS to an LRS. Additionally, the current generated by the second small pulse is slightly larger than the current generated by the third small pulse, which shows the relaxation behavior.[46,47] This behavior is observed more than 50 times, as depicted in Fig. S2,† demonstrating the uniformity of the current over time, which is crucial for applications. Furthermore, the device-to-device variations in I–V curves and the current response under single pulse stimulation were evaluated by 16 devices as shown in Fig. S3.† This indicates that the fabrication process and electrical performances of out Ta/IGZO/TaO_x/Pt dynamic memristors are reproducible. The thicknesses for TaO_x and IGZO were changed and discussed in Fig. S4.†

The nonlinear behavior plays a vital role in RC applications. Notably, the memristor is an inherent nonlinear system, as reflected in the nonlinear equations.[48,49] Here we show the nonlinear response to programming using several tests. Fig. 1d depicts the current response of the device under a

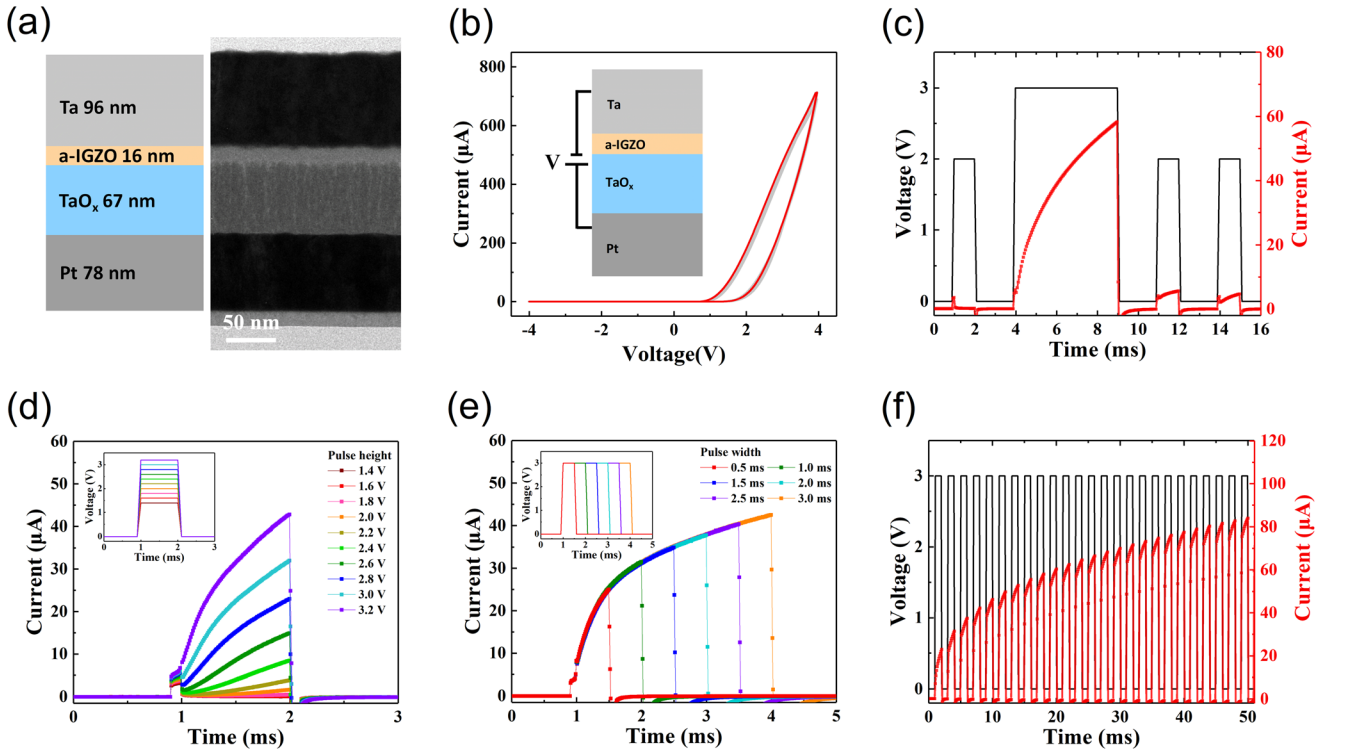

Fig. 1 Microstructural characterization and electrical response of the Ta/IGZO/TaO_x/Pt memristor. (a) The left panel illustrates a schematic representation of the IGZO/TaO_x structure positioned between the Ta and Pt electrodes, along with the thickness of each layer. The right panel displays the corresponding cross-sectional TEM image of the device. (b) Current–voltage (*I*–*V*) characteristics of the device is repeated 20 cycles, and the inset depicts the device structure under bias. (c) The measured current response demonstrates RS and relaxation behaviors. Before the device is turned on, the initial high-resistant state (HRS) is measured under a small pulse (2 V, 1 ms). After the application of a voltage pulse (3 V, 5 ms), the device switches to a low-resistance state (LRS) under small pulses (2 V, 1 ms). (d) The current responses are measured for 1 ms under different amplitudes of input pulses (1 ms) ranging from 1.4 V to 3.2 V with a step of 0.2 V. (e) The measured current responses are depicted for different input pulse widths from 500 μs to 3 ms, where the pulse amplitude is 3 V. (f) The current response is recorded for 25 consecutive voltage pulses (3 V, 1 ms) at 1 ms intervals.

single pulse with varying pulse amplitudes. The current responses exhibit small changes until reaching 2 V. Under higher voltages, the current responses exhibit nonlinear increments as the applied voltage linearly increases to 3.2 V. We also verify the nonlinearity by applying a linearly increasing voltage to the device, as shown in Fig. S5.† Furthermore, the resulting current response also exhibits a nonlinear behavior under different pulse widths, as depicted in Fig. 1e. The current displays linear increases for the pulse width below 1 ms, whereas the rate of the current increase gradually declines with longer pulse widths. To further investigate the nonlinear behavior of the device, continuous positive programming pulses are applied to the device at 50 Hz. Initially, the current increases rapidly, but it gradually saturates with an increasing number of programming pulses, as shown in Fig. 1f. During prolonged programming, the migration of oxygen vacancies in the switching layer is triggered. The loss of the programming capability at high-conductance states can be attributed to the more pronounced relaxation effect in the switching layer.[50–52] The relaxation effect can be considered in the rate equation of the state variable (w) of the device, which will be discussed in Fig. 2.

Simulation results

The memristive behavior is based on the V_{ox} movement inside the TaO_x layer.[45] Briefly, the memristive effects and nonlinearity shown in Fig. 1 are caused by the redistribution of oxygen vacancies near the TaO_x/IGZO interface.[53] These behaviors are further verified using the compact model of the dynamic memristor as follows:[51]

$$I = w\gamma \sinh(\delta V) + (1 - w)\, a[1 - \exp(-\beta V)] \quad (1)$$

$$dw/dt = \lambda \sinh(\eta V) - w/\tau \quad (2)$$

The carrier transport at the IGZO/TaO_x interface is governed by two processes: (I) thermal agitation of electrons and (II) tunneling of electrons from IGZO toward TaO_x. Eqn (1) represents the current–voltage relationship based on the state variable (w), which incorporates the conduction channel in two aspects: The first term represents the tunneling behavior at the IGZO/TaO_x interface, and the second term demonstrates Schottky-like emission behaviors.[54–56] The device conductance can be affected by the state variable (w), which is the relative weight of the two processes due to the movement of oxygen vacancies. Upon the application of a positive voltage at the BE,

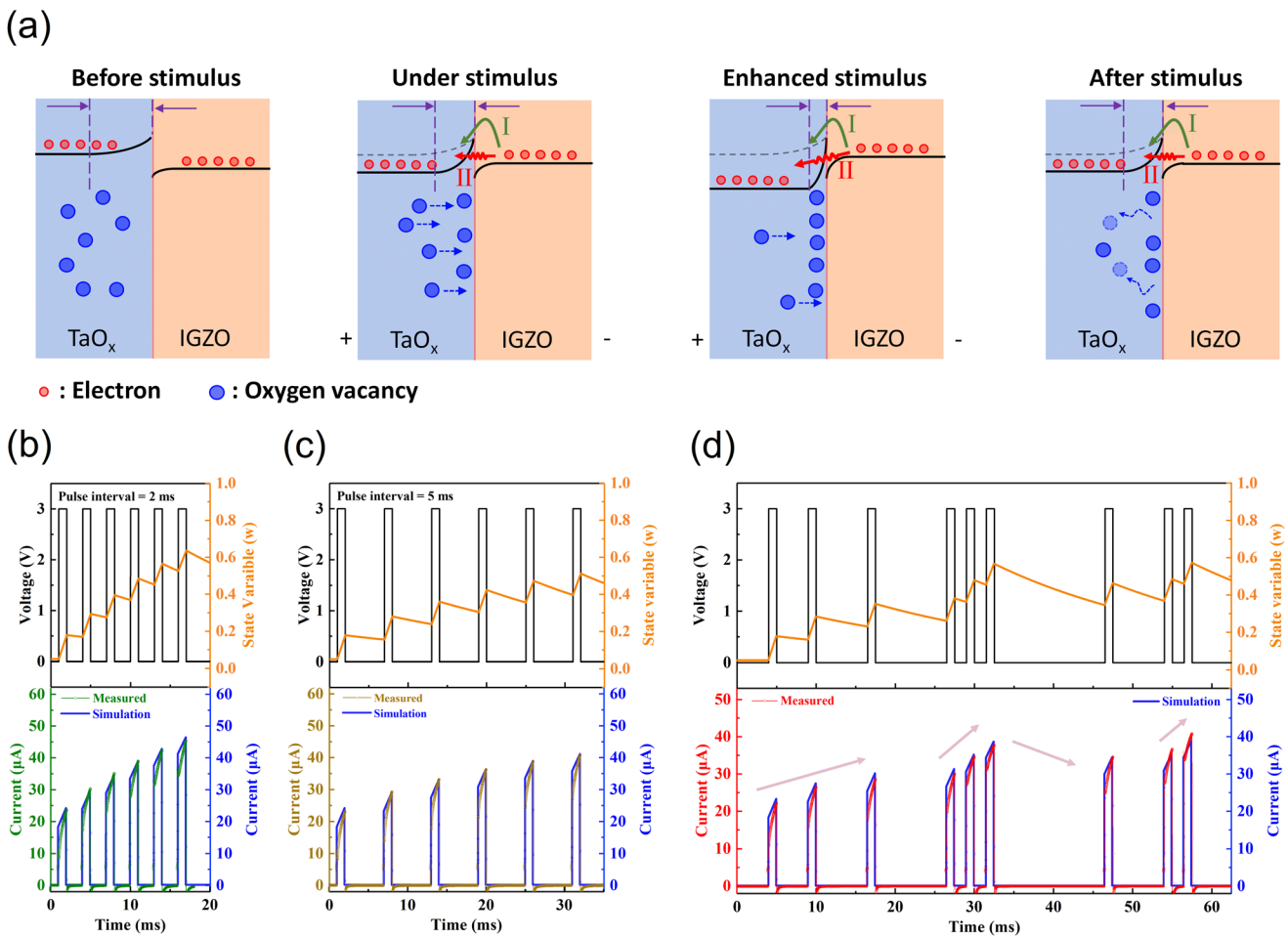

Fig. 2 Schematic of carrier transport and simulation results based on the memristor model describing the dynamic behavior of the IGZO/TaO_x-based memristor. (a) Underlying working mechanism of the memristor. The relocation of positively charged oxygen vacancies within TaO_x leads to a dynamic change in conductance upon the change in depletion width. The main conduction mechanism: (I) the thermal excitation of electrons from IGZO to TaO_x occurs owing to the conduction band offset, and (II) the tunneling process occurs as electrons from the conduction band of IGZO tunnel through the barrier to TaO_x. (b and c) The curves in the top subfigures represent different voltage waveforms (black curve) and the dynamic change in the state variable (w, orange curve). The bottom subfigures represent the measured (green curve in (b) and dark yellow curve in (c)) and simulated (blue curve) current responses under different pulse intervals. Consecutive pulses result in an increase in both the state variable (w) and the current response. Additionally, as the pulse interval increases, the enhancement is suppressed. (d) The trend of the measured current under a random temporal input pulse is consistent with the simulation results.

the electric field can drive the migration of oxygen vacancies toward the IGZO/TaO_x interface, resulting in the accumulation of oxygen vacancies. This leads to Ohmic-like contact dominated by a tunneling current and increases the state variable (w).[57] Eqn (2) represents the dynamic behavior of the state variable (w), which includes two factors: The first factor is the effect of the applied voltage, which can drift V_{ox}, and the second factor is the effect of decay with effective time constant (τ) due to the spontaneous relaxation of V_{ox}. This model is effectively employed to simulate the electrical behavior of the IGZO/TaO_x-based memristor. The fitting parameters α, β, γ, δ, λ, η, τ in eqn (1) and (2) are provided in Table S2.† To simulate device responses to input pulses, the pulse parameters such as voltage amplitude, width, and pulse interval are used in eqn (1) and (2)

The schematic diagram of the relocation of oxygen vacancies is shown in Fig. 2a to illustrate the memristor model. The band diagram was plotted through the analysis of ultraviolet photoelectron spectroscopy (UPS) and ultraviolet-visible (UV-vis) spectrophotometer as shown in Fig. S6–S8.† Sufficient voltage (>2 V) must be applied to the BE to drift the oxygen vacancies in TaO_x toward the TaO_x/IGZO interface. This makes the depletion region at the TaO_x side narrower, and thereby enhances the tunneling probability for electrons from IGZO layer to TaOx layer.[30,58,59] Therefore, the current rises dramatically, and the resistive state gradually switches to an LRS. Upon further increasing the voltage, the transport of electrons is dominated by tunneling, indicating the state variable (w) increases. When oxygen vacancies are accumulated at the IGZO/TaO_x interface[60] right after the electrical stimulus, the

mobile oxygen vacancies retain temporarily and progressively relax back to the TaO_x layer because of the concentration gradient, causing the upward-band-bending depletion region at TaO_x side to be widened. Therefore, the tunneling current and the state variable (w) decrease, leading to the decay of the current to an HRS once the stimulation pulse is removed.[50,61] Taking advantage of the band offset between the two oxides and the dynamic relocation of oxygen vacancies and carriers, this bilayered metal oxide-based memristor is capable of demonstrating resistive switching and short-term memory (STM) characteristics.

To verify the agreement between the experimental results and modelling functions, we used six pulses (3 V, 1 ms) with different time intervals (2 and 5 ms). The measured and simulation results show that the current response gradually increases, as shown in Fig. 2b. As the time interval between electrical pulses increases (from 2 ms to 5 ms), the change in the potentiated current significantly decreases, as shown in Fig. 2c. Fig. S9† displayed transient current responses under other pulse interval conditions (with pulse interval 0.5, 1 and 3 ms). As the pulse interval increases, the experimentally measured current responses decrease. The corresponding simulated currents decrease due to the relaxation of the state variable based on the memristor model. In particular, the change in the device current under different pulse intervals can be quantitatively explained using simulations based on the memristor model. Furthermore, as shown in Fig. 2d, as the pulses are applied at a high rate, the state variable (w) gets larger, leading to a rapid increase in the device current. Conversely, when the pulses are applied at a low rate, the longer pulse interval allows more time for the state variable (w) to decrease, reducing the device current. Fig. S10† demonstrated the consistency of the dynamic changes between the measured currents and state variables subject to the pulse streams of decreasing and increasing pulse number. As shown in Fig. S10a,† the current and state variable were escalated consistently when receiving the first stream of the electrical stimulation (four pulses). Later, the subsequent pulse streams (three, two and one pulses) applied after a time interval did not potentiate the conductance state appreciably. This implies that the initial four pulses strengthen the conductance to a higher level and intrigues the relaxation of state variable (oxygen vacancies), which compromises the stimulation of subsequent pulse streams with descending pulse numbers. Conversely, Fig. S10b† exhibits the increasing currents and state variable responses under the application of pulse streams of increasing pulse number (from one to four pulses). The potentiated results illustrate that the stimulation of incremental pulse numbers surpasses the relaxation effect since the initial state variable is lower. This demonstration also specifies that the current responses differ when the pulse sequences are varied. The current and the state variable (w) of the memristor are sensitive to the application and removal of electrical stimuli, resulting in different transient responses, which can be useful for training sequential dependent signals in neural networks. Moreover, the memristor exhibits analog RS capabilities with multilevel states, enabling the generation of diverse reservoir states.[62,63]

STM analysis of device

Notably, when a positive bias is applied to the BE, the conductance gradually increases, indicating potentiation, as shown in Fig. 3a. However, it shows that the I–V curves overlap as the voltage sweeps consecutively. This suggests the memory effect fades over time. The decay of w, as discussed earlier, provides a direct explanation for this phenomenon. Memristive devices with STM are better suited to process temporally encoded input patterns.[47,64] Elements of a reservoir layer in RC should ideally possess an STM property. Fig. 3b depicts how the STM effect plays a crucial role in extracting temporal features from the input pulse stream.[65] When subjected to sequential inputs, the device exhibits a nonlinear transient response attributed to the STM effect. By aligning the measurement parameters and decay time appropriately, the captured dynamical device state is recorded using fixed time steps, generating nodes that represent reservoir states. These nodes are then utilized to map time-series data and analyze extracted features within PRC.[66]

The STM effect of the IGZO/TaOx-based memristor was further investigated by examining three pulse trains with varying pulse arrangements, as depicted in Fig. 3c. This figure demonstrates the impact of recent inputs on the present response of the memristors. In the cases labeled as 1_111, 11_11, and 111_1, the different numbers of pulse stimulations (3 V, 1 ms) before the symbol "_" led to different responses. However, the state variable (w) exhibites varying rates of decline over the 20 ms interval, effectively suppressing the conductance with different slopes. This behavior can be attributed to the accumulation of different amounts of oxygen vacancies at the IGZO/TaO_x interface under different pulse arrangements. Consequently, the rate at which oxygen vacancies tend to diffuse back to their original positions during spontaneous relaxation differs. Due to the different nonlinear transient responses observed over the 20 ms interval, the final state of the temporal frame differs among these three cases.

Memristor-based physical reservoir

RC is an efficient network for processing temporal signals, offering lower training costs compared with standard RNNs. Fig. 4a illustrates the schematic of a memristor-based RC system. The reservoir layer captures and processes intricate temporal patterns within the input signal, while the readout layer interprets reservoir states to generate the desired output.

We employ the virtual node concept in the implementation of the reservoir layer in the fabricated memristor device.[66] Instead of mapping the input signal to a feature space using multiple nonlinear units, the virtual node concept utilizes delayed feedback on a single physical device with STM effects. This effect can be observed in the IGZO/TaO_x-based memristor owing to the internal dynamics without having to use recurrent connects in the network. The device exhibits a wide range of transient current responses that can be modulated based on

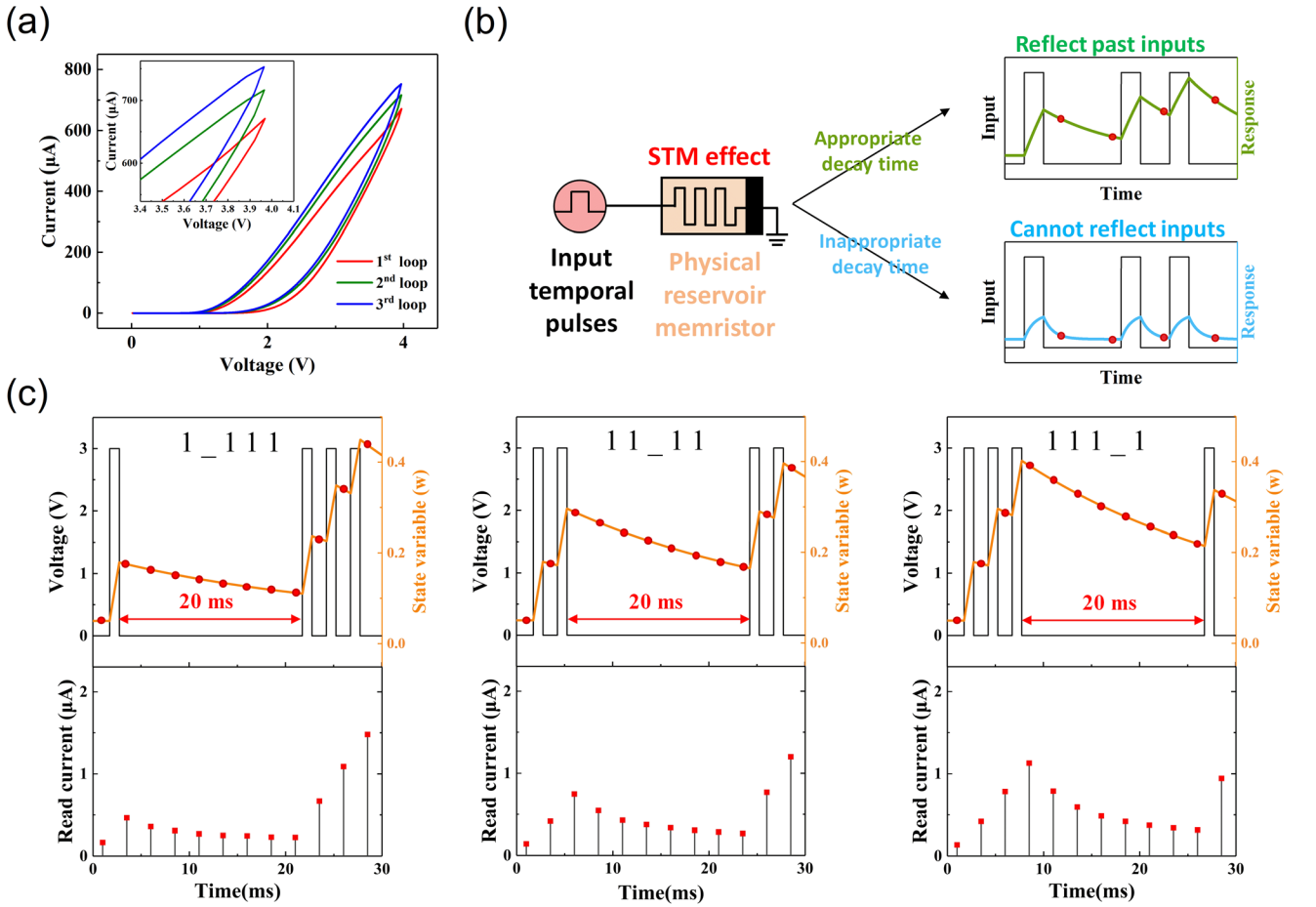

Fig. 3 STM analysis of device. (a) *I*–*V* curve of the Ta/IGZO/TaO_x/Pt memristor from three consecutive positive voltage sweeps (0.0 V → 4.0 V → 0.0 V). Positive voltage sweeps increase the memristor conductance gradually. The inset shows the overlap of adjacent hysteresis loops. (b) The schematic diagram of the STM property ensures that the reservoir state is influenced by recent-past inputs, allowing for the equivalent implementation of neural networks with recursive connections. (c) The dynamic responses of the device are examined under four identical stimulation pulses (3 V, 1 ms) with different sequential arrangements. The symbol "1" denotes the occurrence of a voltage pulse (3 V, 1 ms), whereas the symbol "_" illustrates a long pulse interval (20 ms). Upper panel: The simulation results illustrate the change in the state variable (*w*), which is obtained using the memristor model under three different pulse conditions. Lower panel: dynamic responses of the memristor to pulse sequences measured by the read pulse (1.8 V, 0.5 ms).

the history of external stimulation. These adjustable conductance properties of the memristor serve as reservoir states for mapping feature information from different sequential inputs.

In this study, the device is subjected to four different spike train types: "Tonic", "Bursting", "Adapting", and "Irregular" as shown in Fig. 4b–e. The "Tonic" pattern comprises low-frequency spikes with a constant interval, whereas the "Bursting" pattern includes multiple groups of high-frequency spikes with a constant intergroup interval. The "Adapting" pattern exhibits spikes with gradually increasing intervals, and the "Irregular" pattern represents irregularly firing spikes. The distinct current responses to the four spike train types which demonstrate the capability to effectively analyze the temporal dynamics of neural firing patterns.

Fig. 5a presents the schematic diagram of the RC framework applied to process the binary handwritten image classification. First, the input images go through a preprocessing stage. During this step, each long row of pixels in binary digital images are divided into 7 smaller sections, each containing 4 pixels, resulting in a total of 196 sections (7 sections per row multiplied by 28 rows). Each 4-bit section has 2^4 possible pattern combinations, which are encoded into 16 different pulse sequences before being fed into the reservoir. The RC framework comprises a reservoir and a readout layer. The former does not need any training, whereas the latter is trained using a 196 × 10 single-layer network. Contrarily, the traditional NN is a 784 × 10 single-layer network needed in binary handwritten image classification, which is four times larger than its size. This leads to significantly higher costs in terms of computation. In our study, we evaluate the separability of the memristor by applying pulse streams with various temporal features (Fig. 5b). Fig. 5c depicts the diverse but deterministic output current responses of 16 different input signals with nearly the same initial state. For each pulse sequence, distinct reservoir

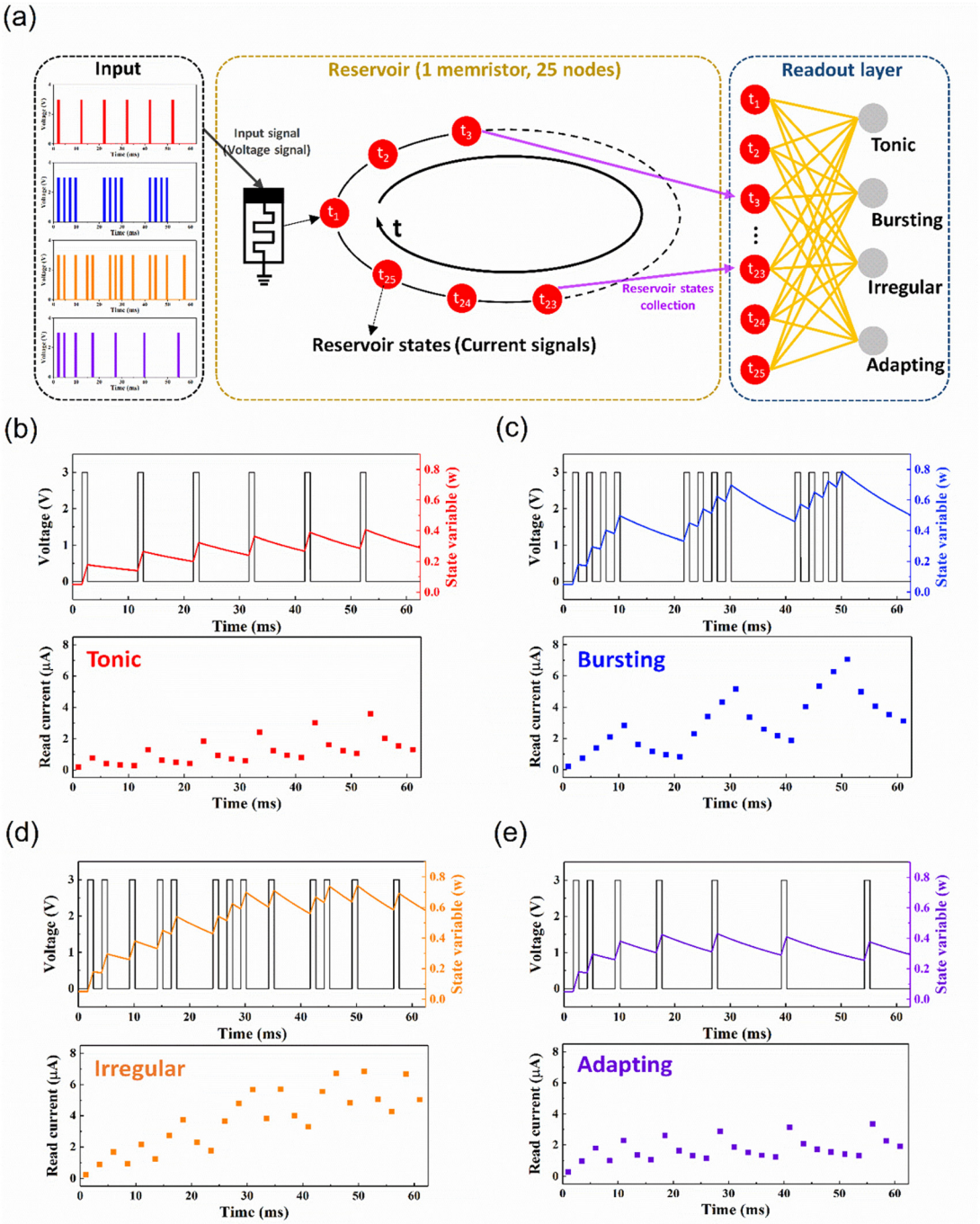

Fig. 4 The schematic illustrates the concept of a memristor-based physical reservoir utilized for time-series data mapping and extracted feature analysis by generating various temporal responses to neural activities. (The classification task in the readout layer was not carried out in this work.) (a) A PRC system architecture comprises the input, reservoir, and readout layer. An input pulse stream is fed into the memristor. The current signals are measured every 2.5 ms by the read pulse (1.8 V, 0.5 ms), which serve as reservoir states, and processed in the readout part. (b–e) Upper panel: simulation results of the state variable (*w*) under different input patterns – "tonic", "bursting", "irregular", and "adapting". Lower panel: the memristor exhibits temporal current responses corresponding to different input patterns.

states measured at the end of the pulse stream are observed, demonstrating the ability to distinguish the 4-bit s. This proves the potential of the device for utilization in an RC-based network. Additionally, Fig. 5d displays the output response of four input signals, [1 0 0 1], [1 0 1 0], [0 1 0 1], and [1 0 1 1], which are repeated 30 times in the same cell. The oxide interface of the device endows it with enhanced stability and reduced cycle-to-cycle variations.[67] These properties significantly contribute to the overall performance and reliability of the memristor-based RC framework.

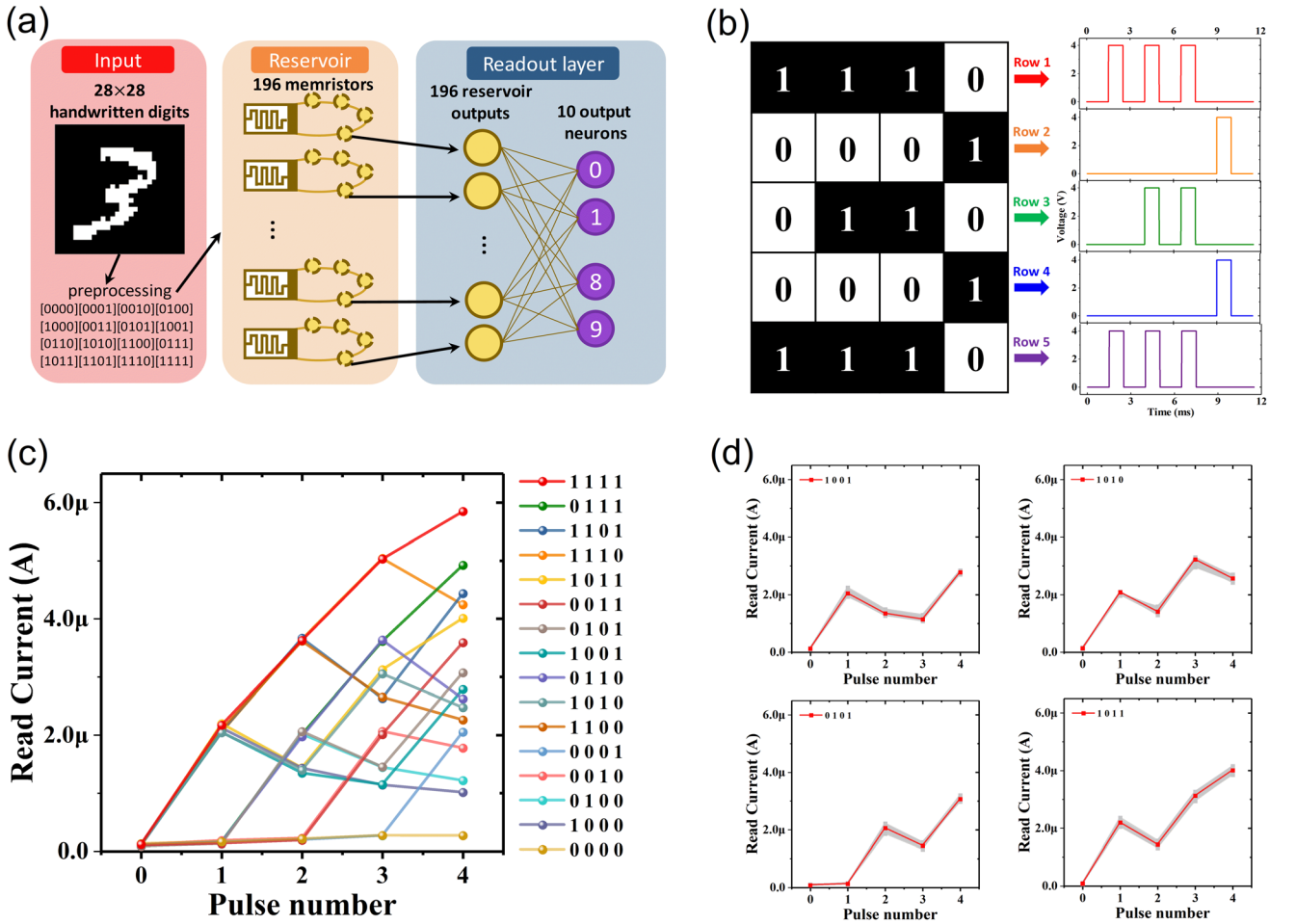

Fig. 5 The IGZO/TaO$_x$-based memristor shows significant reliability and ability to distinguish 4-bit inputs (from "0000" to "1111"). (a) The schematic representation illustrates the RC framework utilizing dynamic memristors as the reservoir and the readout network for processing and classifying binary handwritten digits. The preprocessing stage involves dividing the binary handwritten digit into smaller sections (a row of 28 pixels is divided into 7 sections, and each section contains 4 pixels). These sections are then fed into the dynamic memristor reservoir by pulse streams. Please note that the readout layer was not implemented in this work. (b) As an example, pattern "3" is represented by 20 pixels using 5 × 4-bit inputs during the preprocessing stage. Each row corresponds to a pulse stream, and the pulse (4 V, 1 ms) is used to represent "1", whereas zero voltage represents "0". (c) The separation of 4-bit inputs is achieved through different current responses to 16 specific pulse streams. The reservoir states are reflected as the read currents of the memristors forming the reservoir. The current is measured using a read pulse (2 V, 0.5 ms). (d) The cycle-to-cycle variation is measured by repetitively applying specific pulse streams 30 times on a single device. The variations in the final conductance are 1.58% for "1001", 3.05% for "1010", 1.99% for "0101", and 1.94% for "1011".

Conclusions

Our findings show that the IGZO/TaOx-based memristor holds significant potential for implementation in memristor-based RC systems. Additionally, we conducted simulations of dynamic RS and validated the results with the experimental data using a compact memristor model. We investigated the electrical performance where the state variable (w) can be modulated based on the migration of oxygen vacancies. The nonlinear dynamic current response and the STM behavior were demonstrated in the variations of current levels upon the application and removal of electrical stimuli. These characteristics make the memristor suitable for deployment as an effective physical reservoir. The transient current response of the memristor within a specific duration can serve as the reservoir state, enabling the extraction and analysis of temporal input data. The systematic study on the RS mechanism and device modeling in this work can provide valuable guidance for further optimization and application of dynamic memristors in the RC framework.

Method

In this study, a bilayer oxide-based Ta/IGZO/TaO$_x$/Pt memristor was fabricated on a SiO$_2$/Si substrate, which was cleaned using the RCA process. The BE was fabricated by depositing a Pt film onto a SiO$_2$/Si substrate using DC magnetron sputtering with a

Pt target (99.99%) and the following experimental parameters: sputtering power, 100 W; working pressure, 4 mTorr; Ar flow, 50 sccm. A 67 nm TaO_x layer was then deposited using RF sputtering (target: high-purity Ta (99.99%), sputtering power: 80 W, working pressure: 16 mTorr, mixed gas flow: 50 sccm, and $Ar:O_2$ ratio: 4 : 1). Further, a 16 nm IGZO film was deposited using an IGZO target and RF magnetron sputtering (sputtering power: 50 W, working pressure: 8 mTorr, and Ar flow: 100 sccm). Lastly, a high-purity Ta target was used to pattern the TE using DC magnetron sputtering with a shadow mask ($200 \times 200\ \mu m^2$), and the following parameters were used for deposition: sputtering power, 60 W; working pressure, 7 mTorr; Ar flow, 50 sccm. Electrical characterizations were performed using a Keysight B1500A semiconductor device analyzer. Pulse measurements were performed using a Keysight wave generator fast measurement unit. Further, microstructural characterization was performed using TEM (JEM-2100F field-emission tunneling electron microscope). Python was used to fit and validate the compact memristor model.

Author contributions

Bo-Ru Lai: conceptualization, data curation, formal analysis, investigation, methodology, software, writing – original draft. Kuan-Ting Chen: data curation, formal analysis, investigation, methodology, software, writing –original draft. Rajneesh Chaurasiya: formal analysis, investigation, writing–original draft. Song-Xian You: conceptualization, data curation, formal analysis, investigation, writing – review & editing. Wen-Dung Hsu: investigation, software, supervision, writing – review & editing. Jen-Sue Chen: formal analysis, funding acquisition, project administration, resources, supervision, visualization, writing – review & editing.

Conflicts of interest

There are no conflicts to declare.

Acknowledgements

We appreciate the financial support from the National Science and Technology Council of Taiwan (Project No. NSTC 112-2223-E-006-010 and NSTC 112-2926-I-006-502-G). This research was also supported in part by Higher Education Sprout Project, Ministry of Education to the Headquarters of University Advancement at National Cheng Kung University (NCKU).

References

1 Z. Cao, B. Sun, G. Zhou, S. Mao, S. Zhu, J. Zhang, C. Ke, Y. Zhao and J. Shao, *Nanoscale Horiz.*, 2023, **8**, 716–745.
2 S.-O. Park, T. Park, H. Jeong, S. Hong, S. Seo, Y. Kwon, J. Lee and S. Choi, *Nanoscale Horiz.*, 2023, **8**, 1366–1376.
3 J. Li, H. Abbas, D. S. Ang, A. Ali and X. Ju, *Nanoscale Horiz.*, 2023, **8**, 1456–1484.
4 D. N. Levine, *J. Neurol. Sci.*, 2007, **253**, 1–6.
5 A. E. Pereda, *Nat. Rev. Neurosci.*, 2014, **15**, 250–263.
6 C. Koch and G. Laurent, *Science*, 1999, **284**, 96–98.
7 S. Ren, K. He, R. Girshick and J. Sun, *IEEE Trans. Pattern Anal. Mach. Intell.*, 2017, **39**, 1137–1149.
8 A. Esteva, B. Kuprel, R. A. Novoa, J. Ko, S. M. Swetter, H. M. Blau and S. Thrun, *Nature*, 2017, **542**, 115–118.
9 L. Deng, J. Li, J. T. Huang, K. Yao, D. Yu, F. Seide, M. Seltzer, G. Zweig, X. He, J. Williams, Y. Gong and A. Acero, 2013 IEEE International Conference on Acoustics, Speech and Signal Processing, 2013, 8604–8608.
10 T. Brown, B. Mann, N. Ryder, M. Subbiah, J. D. Kaplan, P. Dhariwal, A. Neelakantan, P. Shyam, G. Sastry and A. Askell, *Adv. Neural Inf. Process. Syst.*, 2020, **33**, 1877–1901.
11 D. Silver, A. Huang, C. J. Maddison, A. Guez, L. Sifre, G. van den Driessche, J. Schrittwieser, I. Antonoglou, V. Panneershelvam, M. Lanctot, S. Dieleman, D. Grewe, J. Nham, N. Kalchbrenner, I. Sutskever, T. Lillicrap, M. Leach, K. Kavukcuoglu, T. Graepel and D. Hassabis, *Nature*, 2016, **529**, 484–489.
12 A. Sherstinsky, *Physica D*, 2020, **404**, 132306.
13 H. Salehinejad, S. Sankar, J. Barfett, E. Colak and S. Valaee, *arXiv*, 2015, preprint, arXiv:1801.01078, DOI: **10.48550/arXiv.1801.01078**.
14 R. Pascanu, T. Mikolov and Y. Bengio, International conference on machine learning, 2013, 1310–1318.
15 M. Lukoševičius and H. Jaeger, *Comput. Sci. Rev.*, 2009, **3**, 127–149.
16 S. Shahi, F. H. Fenton and E. M. Cherry, *Mach. Learn. Appl.*, 2022, **8**, 100300.
17 D. Verstraeten, B. Schrauwen and D. Stroobandt, The 2006 IEEE International Joint Conference on Neural Network Proceedings, 2006, 1050–1053.
18 J. Pathak, B. Hunt, M. Girvan, Z. Lu and E. Ott, *Phys. Rev. Lett.*, 2018, **120**, 024102.
19 H. Jaeger and H. Haas, *Science*, 2004, **304**, 78–80.
20 G. Tanaka, T. Yamane, J. B. Héroux, R. Nakane, N. Kanazawa, S. Takeda, H. Numata, D. Nakano and A. Hirose, *Neural Networks*, 2019, **115**, 100–123.
21 K. Nakajima, *Jpn. J. Appl. Phys.*, 2020, **59**, 060501.
22 T. Matsuo, D. Sato, S.-G. Koh, H. Shima, Y. Naitoh, H. Akinaga, T. Itoh, T. Nokami, M. Kobayashi and K. Kinoshita, *ACS Appl. Mater. Interfaces*, 2022, **14**, 36890–36901.
23 S. K. Bose, J. B. Mallinson, E. Galli, S. K. Acharya, C. Minnai, P. J. Bones and S. A. Brown, *Nanoscale Horiz.*, 2022, **7**, 437–445.
24 N. V. Prudnikov, V. A. Kulagin, S. Battistoni, V. A. Demin, V. V. Erokhin and A. V. Emelyanov, *Phys. Status Solidi A*, 2023, **220**, 2200700.

25 C. Du, F. Cai, M. A. Zidan, W. Ma, S. H. Lee and W. D. Lu, *Nat. Commun.*, 2017, **8**, 2204.
26 G. Milano, G. Pedretti, K. Montano, S. Ricci, S. Hashemkhani, L. Boarino, D. Ielmini and C. Ricciardi, *Nat. Mater.*, 2022, **21**, 195–202.
27 R. Midya, Z. Wang, S. Asapu, X. Zhang, M. Rao, W. Song, Y. Zhuo, N. Upadhyay, Q. Xia and J. J. Yang, *Adv. Intell. Syst.*, 2019, **1**, 1900084.
28 A. N. Matsukatova, N. V. Prudnikov, V. A. Kulagin, S. Battistoni, A. A. Minnekhanov, A. D. Trofimov, A. A. Nesmelov, S. A. Zavyalov, Y. N. Malakhova, M. Parmeggiani, A. Ballesio, S. L. Marasso, S. N. Chvalun, V. A. Demin, A. V. Emelyanov and V. Erokhin, *Adv. Intell. Syst.*, 2023, **5**, 2200407.
29 C.-H. Huang, J.-S. Huang, C.-C. Lai, H.-W. Huang, S.-J. Lin and Y.-L. Chueh, *ACS Appl. Mater. Interfaces*, 2013, **5**, 6017–6023.
30 S. D. Ha and S. Ramanathan, *J. Appl. Phys.*, 2011, **110**, 071101.
31 L. Pereira, P. Barquinha, E. Fortunato, R. Martins, D. Kang, C. J. Kim, H. Lim, I. Song and Y. Park, *Thin Solid Films*, 2008, **516**, 1544–1548.
32 R. Vogel, P. Hoyer and H. Weller, *J. Phys. Chem.*, 2002, **98**, 3183–3188.
33 S. Jeong, S. Jang, H. Han, H. Kim and C. Choi, *J. Alloys Compd.*, 2021, **888**, 161440.
34 Y. Magari, S. G. M. Aman, D. Koretomo, K. Masuda, K. Shimpo, H. Makino, M. Kimura and M. Furuta, *ACS Appl. Mater. Interfaces*, 2020, **12**, 47739–47746.
35 F. A. M. Koeck and R. J. Nemanich, *Front. Mech. Eng.*, 2017, **3**, 19.
36 M. Błaszczyszyn, *Surf. Sci.*, 1976, **59**, 533–540.
37 J. Yang, F. Zhang, H.-M. Xiao, Z.-P. Wang, P. Xie, Z. Feng, J. Wang, J. Mao, Y. Zhou and S.-T. Han, *ACS Nano*, 2022, **16**, 21324–21333.
38 S. Zhang, K. Guo, L. Sun, Y. Ni, L. Liu, W. Xu, L. Yang and W. Xu, *Adv. Mater.*, 2021, **33**, 2007350.
39 G. Lucovsky, Y. Zhang, G. B. Rayner, G. Appel, H. Ade and J. L. Whitten, *J. Vac. Sci. Technol. B*, 2002, **20**, 1739–1747.
40 X. Zhu, Q. Wang and W. D. Lu, *Nat. Commun.*, 2020, **11**, 2439.
41 G. Tanaka and R. Nakane, *Sci. Rep.*, 2022, **12**, 9868.
42 Y. H. Jang, S. H. Lee, J. Han, W. Kim, S. K. Shim, S. Cheong, K. S. Woo, J.-K. Han and C. S. Hwang, *Adv. Mater.*, 2023, 2309314.
43 S.-G. Ren, A.-W. Dong, L. Yang, Y.-B. Xue, J.-C. Li, Y.-J. Yu, H.-J. Zhou, W.-B. Zuo, Y. Li, W.-M. Cheng and X.-S. Miao, *Adv. Mater.*, 2023, 2307218.
44 J. H. Yoon, K. M. Kim, S. J. Song, J. Y. Seok, K. J. Yoon, D. E. Kwon, T. H. Park, Y. J. Kwon, X. Shao and C. S. Hwang, *Adv. Mater.*, 2015, **27**, 3811–3816.
45 S. Choi, S. Jang, J.-H. Moon, J. C. Kim, H. Y. Jeong, P. Jang, K.-J. Lee and G. Wang, *NPG Asia Mater.*, 2018, **10**, 1097–1106.
46 T. Chang, S.-H. Jo and W. Lu, *ACS Nano*, 2011, **5**, 7669–7676.
47 Z. Wang, T. Zeng, Y. Ren, Y. Lin, H. Xu, X. Zhao, Y. Liu and D. Ielmini, *Nat. Commun.*, 2020, **11**, 1510.
48 D. B. Strukov, G. S. Snider, D. R. Stewart and R. S. Williams, *Nature*, 2008, **453**, 80–83.
49 K. Yang, J. J. Yang, R. Huang and Y. Yang, *Small Sci.*, 2022, **2**, 2100049.
50 C. Du, W. Ma, T. Chang, P. Sheridan and W. D. Lu, *Adv. Funct. Mater.*, 2015, **25**, 4290–4299.
51 T. Chang, S.-H. Jo, K.-H. Kim, P. Sheridan, S. Gaba and W. Lu, *Appl. Phys. A*, 2011, **102**, 857–863.
52 S.-G. Koh, H. Shima, Y. Naitoh, H. Akinaga and K. Kinoshita, *Sci. Rep.*, 2022, **12**, 6958.
53 X. Li, J. Tang, Q. Zhang, B. Gao, J. J. Yang, S. Song, W. Wu, W. Zhang, P. Yao, N. Deng, L. Deng, Y. Xie, H. Qian and H. Wu, *Nat. Nanotechnol.*, 2020, **15**, 776–782.
54 M. Min, S. Sakri, G. A. Saenz and A. B. Kaul, *ACS Appl. Mater. Interfaces*, 2021, **13**, 5379–5389.
55 G. Zeng, X.-X. Li, Y.-C. Li, D.-B. Chen, Y.-C. Chen, X.-F. Zhao, N. Chen, T.-Y. Wang, D. W. Zhang and H.-L. Lu, *ACS Appl. Mater. Interfaces*, 2022, **14**, 16846–16855.
56 G. Nazir, M. F. Khan, I. Akhtar, K. Akbar, P. Gautam, H. Noh, Y. Seo, S.-H. Chun and J. Eom, *RSC Adv.*, 2017, **7**, 16890–16900.
57 J. J. Yang, M. D. Pickett, X. Li, D. A. A. Ohlberg, D. R. Stewart and R. S. Williams, *Nat. Nanotechnol.*, 2008, **3**, 429–433.
58 M. Hansen, M. Ziegler, L. Kolberg, R. Soni, S. Dirkmann, T. Mussenbrock and H. Kohlstedt, *Sci. Rep.*, 2015, **5**, 13753.
59 A. Sawa, *Mater. Today*, 2008, **11**, 28–36.
60 S. Dirkmann, M. Hansen, M. Ziegler, H. Kohlstedt and T. Mussenbrock, *Sci. Rep.*, 2016, **6**, 35686.
61 Y. B. Nian, J. Strozier, N. J. Wu, X. Chen and A. Ignatiev, *Phys. Rev. Lett.*, 2007, **98**, 146403.
62 J. Cao, X. Zhang, H. Cheng, J. Qiu, X. Liu, M. Wang and Q. Liu, *Nanoscale*, 2022, **14**, 289–298.
63 A. Goudarzi, P. Banda, M. R. Lakin, C. Teuscher and D. Stefanovic, *arXiv*, 2014, preprint, arXiv:1401.2224, DOI: 10.48550/arXiv.1401.2224.
64 W. Zhou, S. Wen, Y. Liu, L. Liu, X. Liu and L. Chen, *Neural Networks*, 2023, **158**, 293–304.
65 K. D. Cantley, R. C. Ivans, A. Subramaniam and E. M. Vogel, 2017 International Joint Conference on Neural Networks (IJCNN), 2017, 4633–4640.
66 L. Appeltant, M. C. Soriano, G. Van der Sande, J. Danckaert, S. Massar, J. Dambre, B. Schrauwen, C. R. Mirasso and I. Fischer, *Nat. Commun.*, 2011, **2**, 468.
67 M. Kim, M. A. Rehman, D. Lee, Y. Wang, D.-H. Lim, M. F. Khan, H. Choi, Q. Y. Shao, J. Suh, H.-S. Lee and H.-H. Park, *ACS Appl. Mater. Interfaces*, 2022, **14**, 44561–44571.